An Initial Electric Motor Rotor Vibration Model

Jordan D. Cluts[1], Brenda S. Henderson[2], and Emma L. Pierson
NASA Glenn Research Center, Cleveland, OH, 44135, USA

Ongoing integration of outrunner brushless electric motors into drones and Advanced Air Mobility aircraft presents a need for accurate acoustic predictions derived from prediction of the motor rotor vibrations. In outrunner motors, the external rotor vibrates and drives the acoustic field. At resonant frequencies of the rotor, the rotor displacements will be the largest. The vibrations can lead to acoustic tones that are relevant to the overall acoustic design of these types of vehicles. This study performs a finite element analysis to assess the modes in two electric motor rotors. This model is then refined into a simple parameterized geometry that can make the same predictions for motors of the same class. A parametric sweep and least-squares-curve fit to the finite element analysis data results in a series of simple curves that can predict the mode shapes and frequencies that are likely to appear in this class of motors without the need for any simulation. The simulations are validated by comparison to acoustic and experimental modal-analysis data.

I. Introduction

Brushless DC electric motors are widely used in a variety of applications including small Unmanned Aircraft Systems (sUAS) and larger Advanced Air Mobility (AAM) vehicles. It has previously been shown that in sUAS vehicles at certain frequencies, tones generated by the motors contribute to the overall noise signature [1]. In ground-based applications these tones can be mitigated by an enclosure around a motor. In aircraft however, the motors are often unenclosed and lack the acoustic attenuation an enclosure provides. There is a need to incorporate a low-fidelity prediction model into system-level prediction tools such as The NASA Aircraft Noise Prediction Program (ANOPP) to assist designers of future electrified propulsion vehicles and allow the consideration of acoustics during initial stages of conceptual and preliminary design. ANOPP is regularly used for frequencies up to 10 kHz, this will be the range targeted for prediction here.

Electric motors can generate noise via four primary mechanisms [2]. The first three are: aerodynamic, such as internal air pumping, mechanical, such as bearing noise, and electronic such as noise generated by electronic switching. The last is magnetic noise, the focus of this paper. Noise is generated by the motor magnetic field in a three-stage process first proposed by Zhu [3, 4, 5, 6] and depicted in Fig. 1, which is based on a diagram by Verdyck and Belmans [7]. The model proposes that electromagnetic field fluctuations impart unsteady loads onto the external motor shell. These forces excite the resonant eigenmodes and frequencies of the shell. The resulting shell surface displacement causes pressure fluctuations that may radiate to the far field. Previous work has shown that, for outrunner motors, vibrations of the semi-cylindrical motor rotor occur at frequencies that match observed acoustic tones [8]. The work presented here focuses on the second stage of this model, highlighted in red in Fig. 1. Section IV presents a Finite Element Analysis (FEA) informed semi-empirical model that predicts mode shape and frequency for rotors of 1-5kW outrunner motors.

Significant effort has been expended to model this sound generation process for motors with an inrunner rotor [2, 9, 10, 11]. These approaches are suitable to determine the eigenfrequencies and mode numbers for the external stator. Finite element analysis has also been successfully applied to model the stator vibrations [12]. For motors with an outrunner rotor, Castano et al. [13] used similar analytical and simulation techniques to predict rotor, rather than stator, modes. While Castano et al. analyze a reluctance machine rather than a brushless permanent magnet motor, the analysis of the rotor is comparable. They find that both analytical and finite element analyses of the rotor predict

[1] AIAA Member
[2] AIAA Associate Fellow

similar natural mode frequencies. This prediction however is a two-dimensional model that considers only a slice of the rotor without the impact of supporting spokes.

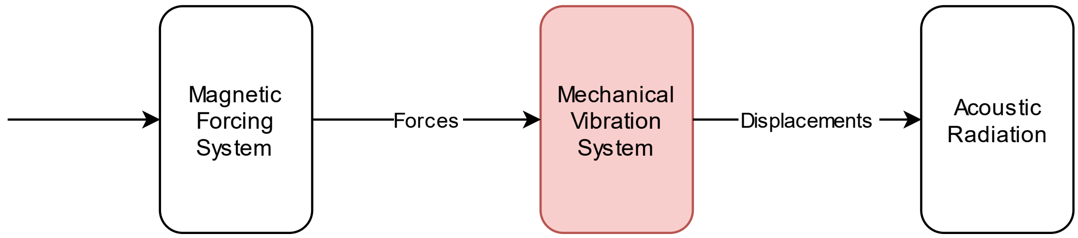

Fig. 1 Three step motor acoustic prediction model derived from Verdyck and Belmans [7].

Numerous analytical models to predict rotor modes and eigenfrequencies based on ideal cylinders have been proposed [14, 15, 16]. Previous attempts to apply analytical models to the motors used in the present study did not successfully reproduce measured frequencies. Despite the success in two-dimensional studies by previous authors and the structural similarity of resulting mode shapes predicted by the analytical theory, the full rotor geometry, in particular the impact of the radial spokes on the end bell, prevents the direct application of these models to these rotors. Furthermore, motors of this class commonly feature high aspect ratios which further increases the impact of the spokes on the resulting eigenfrequencies.

Finite element analysis is a powerful tool that can produce the frequencies, mode shapes, and displacements of rotors but this requires the design details of the motor geometry that would not be available during conceptual system studies. However, it is possible to use the power of FEA to inform a model that can be used in a lower-fidelity approach. This is the approach used here. In this work, we perform finite element analyses of the rotors of two outrunner brushless radial flux DC motors. A parameterized geometry defined by ten key rotor dimensions is then developed. Finite element analysis can then be performed on this simplified geometry without the need to fully model a known rotor. Finally, a semi-empirical model that does not rely on simulation is derived from a parameter sweep of the simplified geometry followed by a least-squares curve fit of the simulation results. The simple curves of this model predict both the frequency and mode shapes of rotor resonant modes for this class of motors.

Section II discusses details of the electric motors used for testing and experimental data collection. Section III presents the finite element modeling process and details of the parameterized model. The results of the modeling efforts and comparisons to experimental modal analysis and acoustic data are provided in Section IV followed by conclusions in Section V.

II. Experiments

A. Motor Description

While there are a variety of types of motors, this effort focuses on brushless DC outrunner motors with a radial flux configuration. A schematic of the motor is shown in Fig. 2. Permanent magnets are positioned on the rotor with the magnetic poles aimed at the axis of rotation as shown in Fig. 2(c). The stator coils are commutated by an electronic speed controller or ESC, eliminating the need for wear components such as brushes, hence the moniker “brushless”. The speed of the motor is controlled by a pulse-width-modulation (PWM) signal supplied to the ESC.

The rotor commonly takes the form of a rotating shell that is directly connected to the motor shaft. This shell is comprised of two parts, an end bell directly connected to the motor shaft and a cantilevered cylindrical shell that is supported by the end bell and onto which the magnets are attached. The vibration of this cantilevered cylindrical shell is the focus of the model developed here. The vibration of rotor is believed to be a major source of acoustic tones produced by these motors during operation.

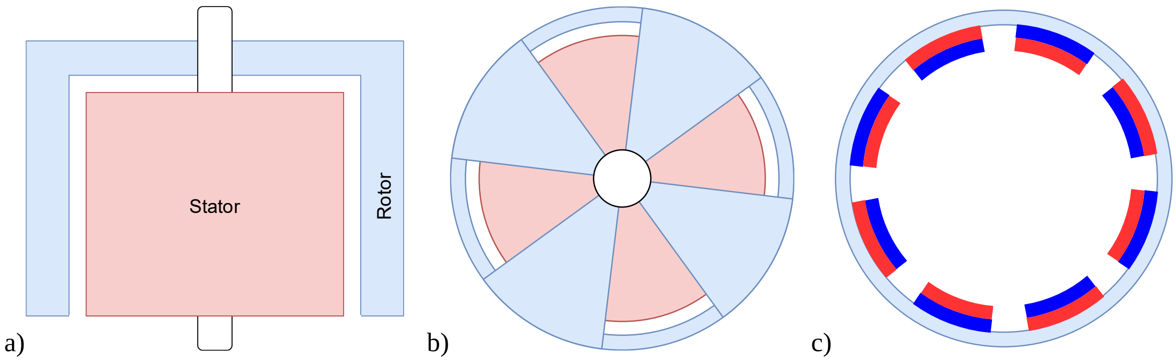

Fig. 2 Outrunner motor configuration (a) cutaway side view (b) top view of an end bell with 4 spokes (c) radial flux magnet arrangement.

The Scorpion SII 4020 and the T-motor U13 are used in the current study due to the differences in their power ratings and motor aspect ratios. Key details, in particular the power rating and aspect ratios of these motors are presented in Table 1. Two motors with different output power are selected to provide a useful range of applicability of the model which will be discussed in Section IV. The range encompassed by these motors is approximately 1-5kW, a range commonly used in sUAS. The difference in aspect ratio (diameter/height) is similarly intentional. The motor aspect ratio is expected to have an impact on the rotor vibrations and so encompassing different values is needed to accurately predict most motors in this class. The end bells of each motor also differ in the number of spokes present. Motors in this class vary in number of spokes and for some the end bell is a plate without individual spokes. The end bell spokes are found to be an important factor in determining the rotor vibration modes in simulation as will be discussed in Section III.

Table 1 Scorpion SII 4020 and T-motor U13 specifications

	Scorpion SII 4020	**T-motor U13**
Power Rating	1500W	3848W
kV rating	420kV	100kV
Diameter	40mm	118.4mm
Height	20mm	21.93mm
Aspect Ratio	2	5.4
Number of Slots	12	18
Number of Magnets	14	24
Number of Spokes	6	5

B. Experimental Modal Analysis

Experimental modal analysis was performed on the rotor of both motors to determine the free vibration resonant mode shapes and frequencies. PCB 352C23 accelerometers were applied to the cylindrical surface of each rotor and along the end bell spokes as shown in Fig. 3. The positioning of the accelerometers was informed by the FEA analysis performed prior to the modal analysis (and discussed in Section III A). Multiple accelerometer mounting locations were tested to explore vibrations of both the cylindrical shell and the rotor spokes. For each configuration the rotor was excited by a PCB Model 086E80 ICP Impact Hammer.

During experimental modal analysis, the impact hammer was used to impart an impulsive force on the rotor. This hammer was equipped with a quart piezoelectric force sensor. The force on the hammer tip and the resulting accelerations of the shell were recorded at equally spaced radial locations on the cylindrical shell and on the spokes. For the T-motor U13, 36 accelerometers were equally spaced on the cylindrical shell and two accelerometers were positioned on each spoke at different radii. Owing to its smaller size, 12 accelerometers were positioned on the cylindrical shell of the Scorpion SII 4020 in two rows of six. Two rows were used both because the aspect ratio allowed for it and because simulations indicated that second order longitudinal modes may be present within the range of interest. A single accelerometer was positioned on each spoke with one additionally placed on the end of the motor shaft. The accelerometers were referenced to the force applied by the impact hammer. Cross correlations were used to determine the mode shape and resonant frequencies were identified from the spectral analysis.

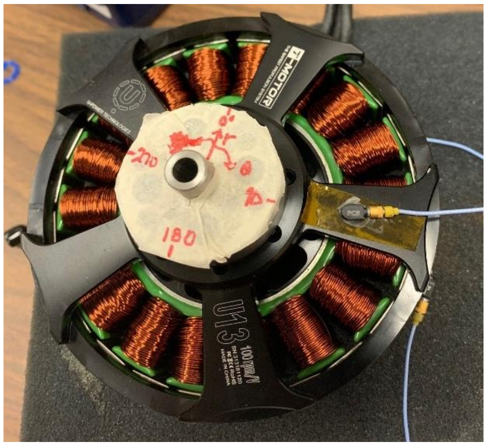

Fig. 3 Accelerometers with blue wire leads attached to T-motor U13.

C. Acoustic Measurements

The acoustic measurements were conducted in the anechoic chamber of the Acoustic Testing Laboratory (ATL) at the NASA Glenn Research Center (see Fig. 4). The chamber has interior dimensions of 6.4 m deep x 5.2 m wide x 5.2 m high. The floor consists of steel grating panels suspended over wedges. The chamber cut-off frequency is 100 Hz.

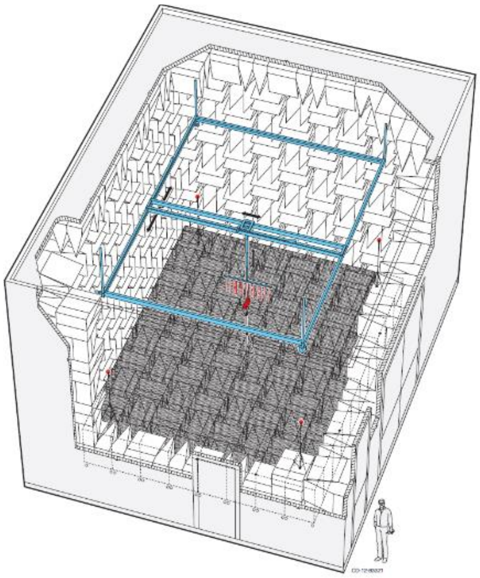

Fig. 4 A schematic of the Acoustic Test Laboratory (ATL) at the NASA Glenn Research Center.

The motors were suspended near the center of the chamber with nylon fishing line to minimize unwanted vibrations and associated sound from the motor mount [see Fig. 5(a)]. Previous motor mounts using a sting were found to produce sound from the motor-sting interface [1] with acoustic levels that were unacceptably high relative to those produced by the motor.

Acoustic measurements were made with the far-field array shown in Fig. 5(b). The array consisted of seven 46AE free-field microphones located on a 1 m radius at 30° increments. Microphone sensitivities were applied to the data.

A T-motor FLAME Series ESC was used with an external PWM signal to control motor speed. The relationship between the PWM signal and the resulting motor speed was unique to each motor and was characterized prior to the acoustic tests. Two types of analyses were conducted and used to identify resonance speeds for the motor and the resulting acoustic radiation at those speeds. The first type of analysis used a programmed PWM signal ramp that resulted in a constant ramp speed for the motor. For this type of acquisition, a tachometer was mounted roughly 1 m from the motor and was used to acquire a tachometer pulse once per revolution. The tachometer signal and acoustic data were acquired continuously throughout the speed ramp at a rate of 200,000 samples/s. The data were later analyzed using conventional order tracking techniques to identify significant orders and the motor speeds that resulted in the peak acoustic radiation for each of those orders. The second type of measurement acquired data at 200,000 samples/s at constant motor speeds for those speeds identified in the order tracking analysis. The frequencies of the dominant tones identified in the resulting spectra were compared with the results of the finite-element and experimental modal analyses as a first step toward associating rotor vibration with the resulting acoustic radiation. The binwidth of the resulting spectra is 6.1035 Hz.

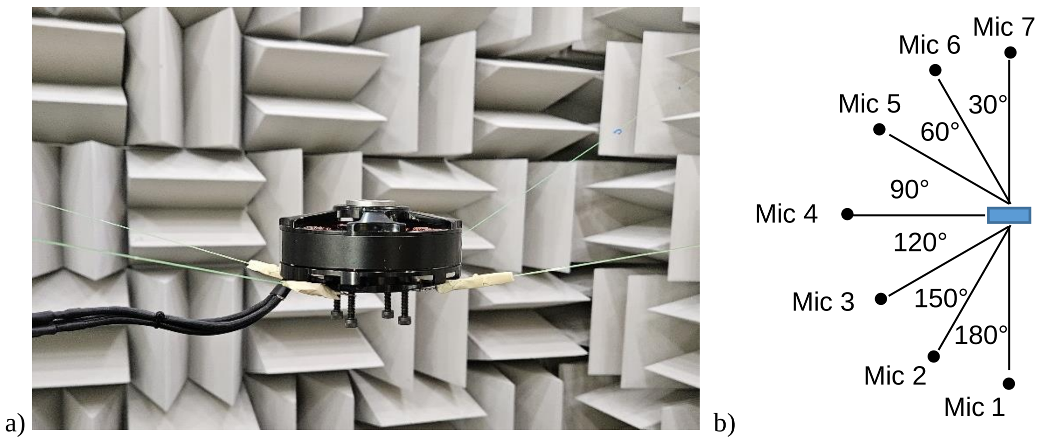

Fig. 5 (a) U13 motor mounted in the ATL (b) Microphone array used in the electric motor noise experiments.

III.   Numerical Methods

A. High Fidelity Simulation

For both the Scorpion SII-4020 and the T-motor U13 motors, a detailed computer model of each rotor geometry was created. A combination of dimensions taken from product manuals and direct measurements of each rotor assembly were used for the model. Each rotor assembly consists of the shaft, end bell spokes, rotor shell, and magnets. Effort was made to capture all details of the actual components including, but not limited to, fillets, mounting holes, and recesses. This process resulted in a CAD assembly that, while not identical to the actual rotor, was sufficient for the FEA analysis presented here. A rendering of the T-motor U13 assembly is shown in Fig. 6(b) alongside a photo of the motor.

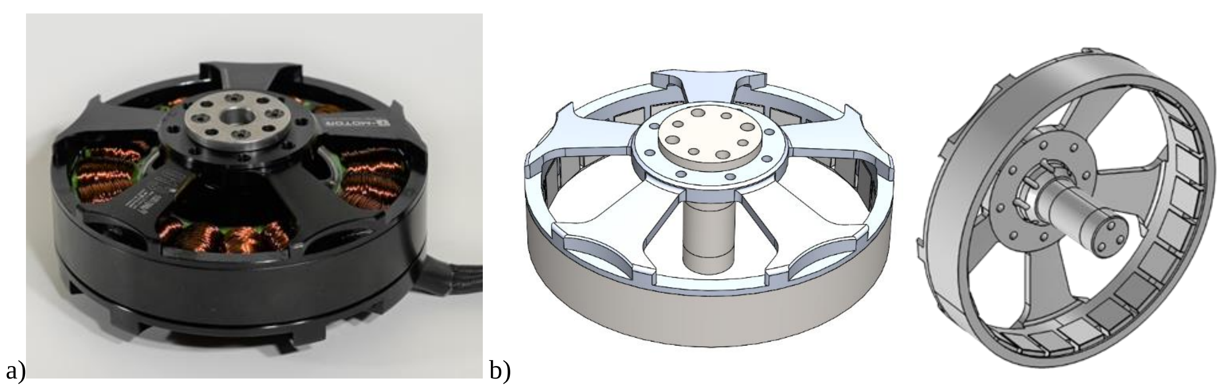

Fig. 6 Photo of (a) T-motor U13 and b) Renderings of corresponding high-fidelity rotor geometry.

Unlike the geometry which can be directly inspected, the material properties of each component were more difficult to determine. A combination of techniques were used to determine the class of materials for each component. The precise alloys remain unknown. The magnets were assumed to be N52 grade NdFeB magnets as this represents the most common high-performance magnet available. The shaft was assumed to be steel as it is the most common material for this application and, in both motors, is ferromagnetic. The rotor shell was likely steel, and the end bell was assumed to be an anodized or enameled aluminum. This assertion was informed primarily by the overall model mass. When this combination of materials was assigned, the overall rotor mass calculated by the modeling software closely matched the measured rotor mass. Other combinations such as a steel end bell resulted in less accurate overall rotor mass. The materials used in the model are summarized in Table 2. For each material, bulk properties of a representative alloy were assigned to the corresponding components. The material properties are listed in Table 3.

Table 2 Rotor Material Components

Component	Material
Magnets	NdFeB N52
Shaft	Steel
Rotor Shell	Steel
End Bell	Aluminum

Table 3 Model Material Properties

Material	Density [kg/m^3]	Young's Modulus [Pa]	Poisson's Ratio
N52 NdFeB	7500	160e9	0.24
Aluminum	2700	70e9	0.33
High-Strength Alloy Steel	7850	200e9	0.3

Each motor geometry was imported into COMSOL Multiphysics for FEA analysis. A bearing surface was used to constrain the geometry. The bearing surface was applied at the bottom and top of the rotor shaft as shown in Fig. 7. These were the locations of the bearings in the motors.

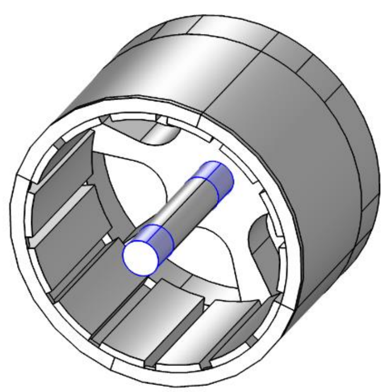

Fig. 7 FEA bearing constraint surface highlighted blue.

Meshing was performed using the automated Free Tetrahedral meshing routine integrated into COMSOL with the element size set to "Normal". A mesh study was performed on the U13 geometry with settings of "Fine" and "Finer". The resulting eigenfrequencies varied by less than 1%, and so "Normal" mesh resolution was used for subsequent simulations.

The model objective was to predict eigenmodes and frequencies of rotors during operation. During operation the rotor is rotating at speeds up to 9,000 rpm and 5,000 rpm for the Scorpion and T-motor respectively. To determine what impact rotation rate had on the predictions, constant speed rotation was added to the FEA study. Calculations at 0, 3000, 6000, and 9000 rpm were performed. For several eigenmodes, the corresponding eigenfrequencies varied by less than 1% with varying rotation rates. This difference is negligible for the purposes of this model so subsequent simulations were performed without rotation.

With the material properties, mesh settings, and impact of rotation established, FEA simulations of each motor were performed. The results of these simulations were used to inform the experimental rotor investigations and validated by comparison to experimental results. For each rotor, several different eigenmodes and frequencies were predicted by the simulation. An example of a rotor displacement of a T-motor eigenmode is depicted in Fig. 8. Based on the depicted displacement, this mode was qualitatively assigned the mode shape M = 2, N = 1 where M is the azimuthal mode number and N is the longitudinal mode number. Subsequently, mode shapes will be described by these two numbers, i.e. the (M,N) mode. Most of the eigenmodes resulting from the simulation were qualitatively assigned an (M,N) mode shape using the computed rotor displacement.

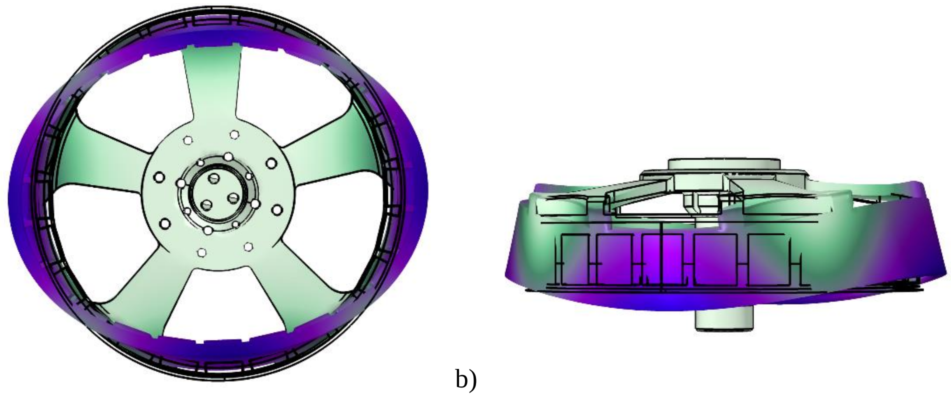

Fig. 8 T-motor U13 1354Hz eigenmode shape (a) bottom view (b) side view

B. Parameterized Geometry Modeling

A simplified parameterized geometry is required for future system level vibration studies to eliminate the need to fully model an extant motor for FEA analysis. The parameterized model was tuned and validated by comparison of mode shape and frequencies to the High-Fidelity FEA simulations. This parameterized geometry must keep only the critical features that affect the resonance modes so that it can be defined by a relatively small number of key dimensions and parameters and generic enough to adequately model rotors which vary in these dimensions. The key features are the rotor shell, spokes, shaft, magnets, and flange. The shell is the primary rotor structural element, and its mass and stiffness must be accurately captured. The spokes significantly alter the stiffness of the shell. Geometry variations that used a solid plate or a fixed number of spokes were found to not match the high-fidelity simulations and so the particular number of spokes was represented in the parametric geometry. The shaft provides the bearing surfaces that constrain the FEA simulation. Lastly, both the magnets and flange alter the mass and stiffness of the overall structure and were required to adequately match the results of the high-fidelity model. Conversely, a number of geometric details were eliminated as they did not play a substantial role in the overall vibrational characteristics. These included bolt holes, chamfers/fillets, and the more complex spoke geometry present in the actual motors.

The resulting parametric geometry is depicted in Fig. 9. Due to the simplicity of this geometry, just ten dimensions or parameters are required to fully define a particular case on which an FEA eigenfrequency and eigenmode analysis can be performed. The ten parameters are detailed in Table 4. The "Magnet Width to Gap Ratio" is defined as the ratio between the width of a single magnet in the circumferential direction and the width of the gap between two adjacent magnets. This parameter characterizes how densely packed the magnets are within the rotor shell. The remaining dimensions are self-explanatory. The parameterized geometry does have several implicit parameters and assumptions. These include details such as the shaft length, and the details surrounding the spoke geometry. Sensitivity studies have shown that the drive shaft length is inconsequential for any reasonable value. The model is sensitive to the geometry of the spokes, but only for changes that substantially affect the spoke stiffness. Small changes in, for example, the internal fillet radius between spokes also had a negligible impact.

The parametric model allows for the rotor of motors of different scales to be easily modeled by applying the corresponding dimensions and parameters. Fig. 10 shows the parametric geometry of both the T-motor and the Scorpion rotors. These motors differ by more than a factor of 3 in power and have very different aspect ratios. Nonetheless, each is represented adequately and the FEA analysis for each matches the corresponding high-fidelity results.

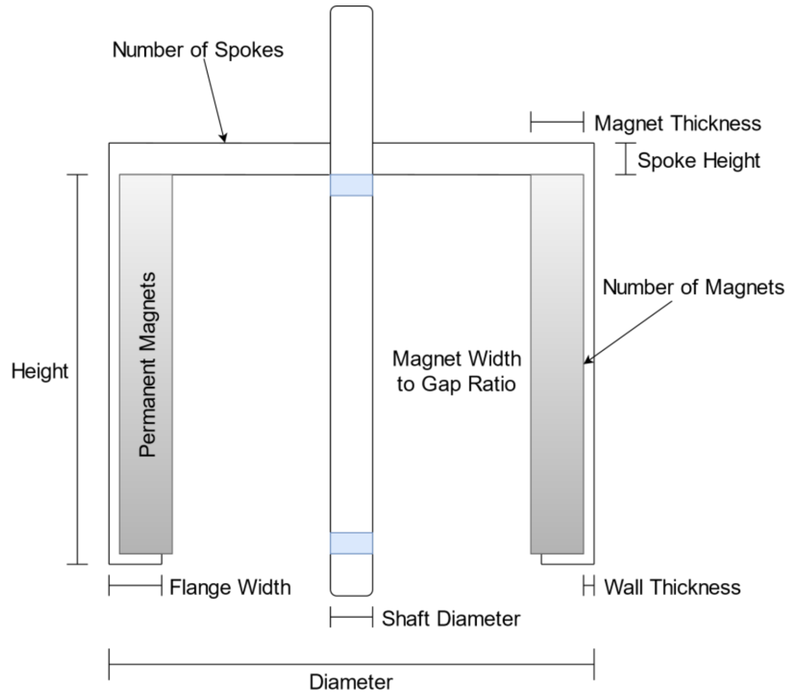

Fig. 9 Illustration of parameterized model with 10 parameters labeled. Bearing interface highlighted in blue.

Table 4 Geometry Parameters

Parameter	**Symbol**
Rotor Diameter	D
Height	H
Wall Thickness	T_W
Magnet Thickness	T_M
Number of Magnets	M
Magnet Width to Gap Ratio	R_M
Number of Spokes	S
Spoke Height	T_S
Flange Width	F
Shaft Diameter	D_S

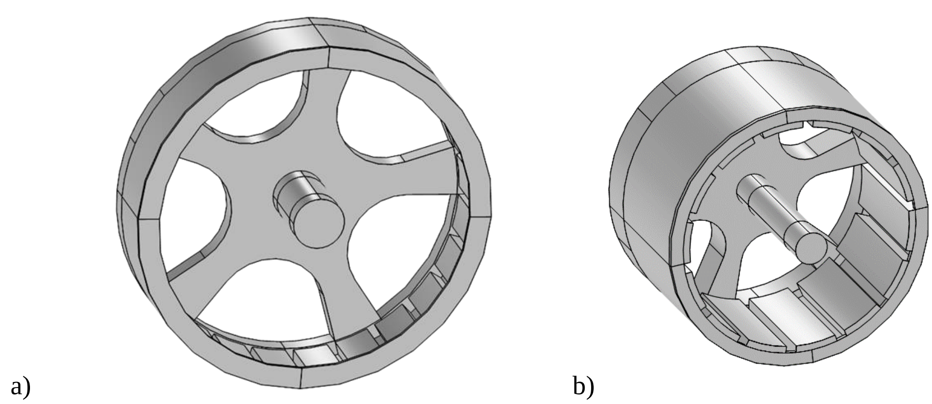

Fig. 10 Parameterized geometry corresponding to (a) the T-motor U13 and (b) Scorpion SII 4020, not to scale.

IV. Results

A. Parameterized Model Validation

To validate the accuracy of the parameterized model, each mode shape can be compared with corresponding mode shapes from the high-fidelity model. For each mode predicted by each model, an (M,N) mode shape is qualitatively assigned by visual inspection. Modes from each model with the same (M,N) mode can then be compared. Fig. 11 depicts the (4,1) mode in the U13 motor using both the high-fidelity and parameterized geometries. The figure makes clear that the mode shapes predicted in these two simulations are qualitatively similar to one another. Beyond the qualitative similarities, the predicted eigenfrequencies can be compared as well. The eigenfrequency of the (4,1) mode for the high-fidelity simulation [Fig. 11(a)] is 5513 Hz. The corresponding eigenfrequency predicted by the parameterized model in Fig. 11(b) is 5685 Hz. The close correspondence between both mode shape and eigenfrequency is evidence the parameterized model is capturing the key physics.

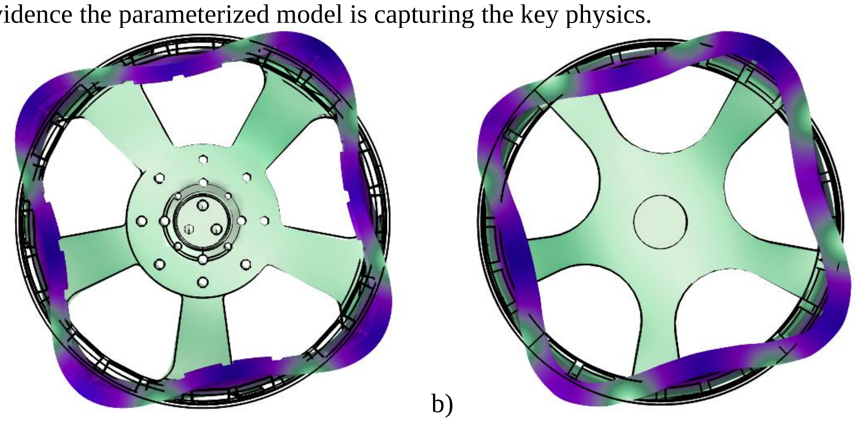

a) b)

Fig. 11 Mode (4,1) in the U13 rotor by a) High Fidelity Geometry and b) Parameterized Geometry.

For each of the modes identified from the results of both simulations the same comparison between high-fidelity and parameterized results can be made. Since the parameterized geometry model is tuned to match the high-fidelity results, we desire the resulting eigenfrequencies to match for all mode shapes within the region of interest. Fig. 12 shows the eigenfrequencies for both models. Modes who's eigenfrequencies are beyond the frequency range of interest are omitted. For most mode shapes, the parameterized model eigenfrequency is within 16% of that predicted by the high-fidelity model.

The tuning process of modifying the parameterized geometry to improve the match with the high-fidelity simulations is required to reach the level of agreement shown in Fig. 12. This tuning does mean that the parameterized model is limited in scope to motors similar to the Scorpion and U13. Motors with larger sizes, higher or lower aspect ratios, or a different electromagnetic configuration are likely to require a retuning of the parameterized geometry. Testing with additional motors both within and beyond the currently studied range would serve to enhance the results presented here.

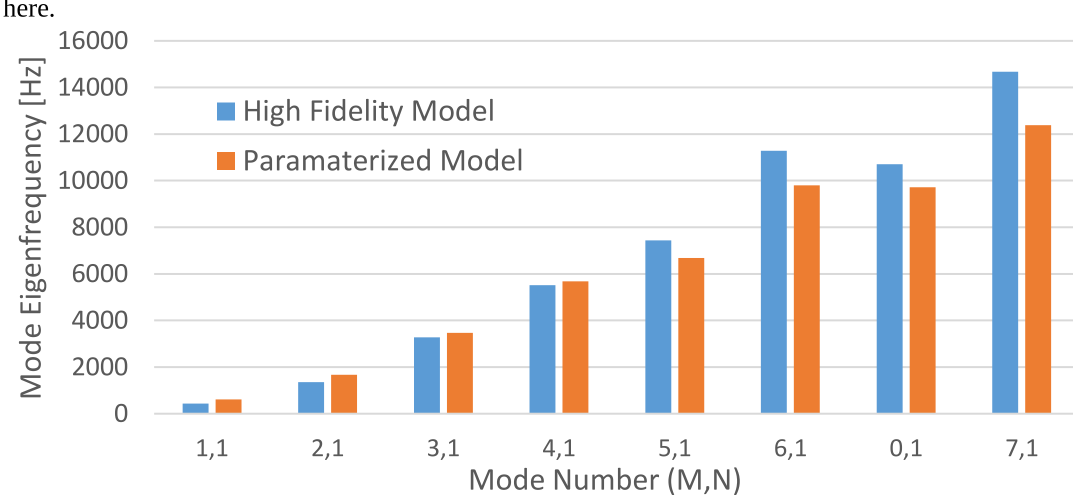

Fig. 12 U13 Eigenfrequency comparison between High-Fidelity FEA and Parameterized FEA.

B. Parametric Sweeps

The parameterized model enables fast geometry generation, allowing exploration of many different geometries more quickly than using hand crafted high-fidelity models. An initial parameter sweep over four of the ten parameters is presented here. The four parameters are the Rotor Diameter, Height, Wall Thickness, and Spoke Height. The latter three are non-dimensionalized to become Aspect Ratio, Wall Thickness Ratio, and Spoke Height Ratio, respectively. The definitions of these dimensionless parameters are provided in Table 5 as well as the range and number of values used in the parametric sweeps. The range of values selected for this sweep roughly correspond to the minimums and maximums of the two motors experimentally tested.

The selected parameter values lead to 3402 different combinations. For each simulation the first 35 eigenmodes are calculated. The selected number of modes ensures that all modes with frequencies in the audible range are identified. For each of the six model parameters that are not selected for the sweep, a constant value is used and is shown in Table 6. The constants are representative of the parameter values for motors studied. Additionally, for Magnet Thickness, Flange Width, and Shaft Diameter, the non-dimensionalized forms are listed.

Table 5 Values in the parametric sweep for each of the four parameters.

	Definition	Minimum	Maximum	Interval	Number of Samples
Rotor Diameter	D	30mm	160mm	5mm	27
Aspect Ratio	D/H	0.7	10	Variable	14
Wall Thickness Ratio	T_W/D	0.02	0.04	0.01	3
Spoke Height Ratio	T_S/H	0.1	0.3	0.1	3

The data in Table 5 shows that most of the points in the parameter space are dedicated to the Rotor Diameter and the Aspect Ratio. These two parameters correspond to the two key dimensions in an analytically ideal cylinder modal analysis. Dedicating most of the parameter space to them makes the best use of computational resources.

The computational resources required for this sweep are moderate. A single engineering workstation with 8 CPU cores with no more than 64 Gb of RAM usage requires approximately 30 hours of computation to complete the 3402 combinations. The work was parallelized to use all available cores. Post processing the data, including the mode-shape categorization that will be described later, requires only a few minutes of computation. The approach is therefore applicable, with moderate computational resources, to a larger number of parameter combinations and to a larger range of parameters if sufficient validation data exists.

Table 6 Minor Parameters Values

	Definition	Value
Magnet Thickness Ratio	T_M/D	0.05
Number of Magnets	M	14
Magnet Width to Gap Ratio	R_M	4
Number of Spokes	S	6
Flange Width Ratio	F/D	0.05
Shaft Diameter Ratio	D_S/D	0.15

C. Mode Identification

Automatically running the many instances of the FEA analysis is relatively straightforward but results in a relatively large amount of data. With 3402 combinations, each of which produces 35 resonant modes, there are over 119,000 mode predictions to process. While the frequency of each mode is directly provided by the analysis, the azimuthal and longitudinal mode shapes (M,N) need to be identified automatically rather than manually.

The FEA generates non-dimensionalized rotor displacement data for each mode. Fig. 13 depicts the displacement for three different modes of the model corresponding to the Scorpion SII 4020. During model development, these mode shapes were identified qualitatively as previously described. To perform this classification automatically, the cylindrical rotor surface is divided into a grid of points with 30 longitudinal stations and 80 circumferential stations for a total of 2400 sampled locations. For each prediction, the 2D Fourier transform is applied to the radial displacement of these 2400 points. The M and N mode number combination with the highest amplitude is the mode shape assigned to that data point. Fig. 13 lists the automatically assigned (M,N) modes for each eigenmode depicted, in each case these correspond to those assigned qualitatively.

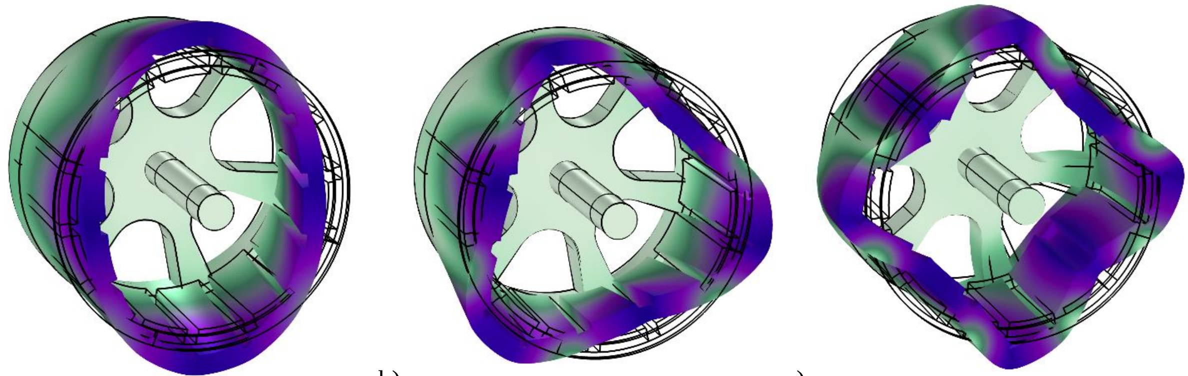

a) b) c)

Fig. 13 Mode Shapes (M,N) (a) (2,1) (b) (3,1) (c) (4,1).

For each of the 119,000 eigenmodes generated by the parameter sweep, the mode shape is identified as described above. Each of the 119,000 datapoints is now comprised of six key pieces of information: the four corresponding geometric parameters, the eigenfrequency, and the (M,N) eigenmode shape. So, there is a 5-dimensional data subset corresponding to each of the different (M,N) modes. Each (M,N) mode will be analyzed individually.

Fig. 14 shows three data points each identified as the (1,1) mode. Fig. 14(d-e) depicts a bottom view of each mode corresponding to Fig. 14(a-c). This view shows that all three points feature the side-to-side motion that corresponds to the (1,1) mode leading to their classification. In contrast the side views in (a-c) show that there are clear differences in the details of the vibration. The (M,N) categorization scheme does not account for these differences.

Each of the three visually distinct modes in Fig. 14 has the same combination of parameters used in the simulation but have different eigenfrequencies with (a) having the lowest frequency, followed by (b) then (c). For the analytical ideal cylinder, each combination of diameter and aspect ratio has a single frequency at which each (M,N) mode shape resonates. Correspondingly, it is expected that within one (M,N) subset, our simulation would produce one data point at one frequency for each parameter combination. The three distinct modes observed in Fig. 14 prove that this expectation does not hold for this simulation. The three different mode shapes are the result of differences between the ideal cylinder and the actual rotor geometry. A more sophisticated model and classification method may be capable of differentiating these modes, but the (M,N) nomenclature does not have adequate granularity to separate these data points.

Fig. 15 depicts a 3-dimensional slice of the 5-dimensional data for the (1,1) mode. The Wall Thickness Ratio and Spoke Height Ratio dimensions are not shown for clarity. Each point in this slice has Wall Thickness Ratio = 0.03 and Spoke Height Ratio = 0.2. The data points in Fig. 14 are taken from Fig. 15. In this depiction, the unique frequency corresponding to each Diameter and Aspect Ratio pair predicted by the analytical theory would create a single surface of points. Fig. 15 however shows three distinct surfaces of points, each spanning most of the Diameter and Aspect Ratio range. The first group, depicted primarily in purple near the bottom of the figure, has the lowest frequency range. The second group begins near 2kHz for large diameters and extends upwards above 10kHz for small diameters. The third group is near the top of the figure. For large diameters it extends from below 10kHz and reaches near 20kHz for smaller diameters.

Fig. 16 shows mode shapes for 3 different points within the lowest frequency of these three groups. Fig. 16(b) is in fact the same data point as Fig. 14(a) and (d). Each of the three points exhibit the same vibration mode despite the large differences in diameter and aspect ratio. The vibration, which manifests over time as a back-and-forth rocking, is correctly identified as the (1,1) mode shape in all three cases. This matches the intuition that points within a single group should have qualitatively the same mode despite having other geometric differences.

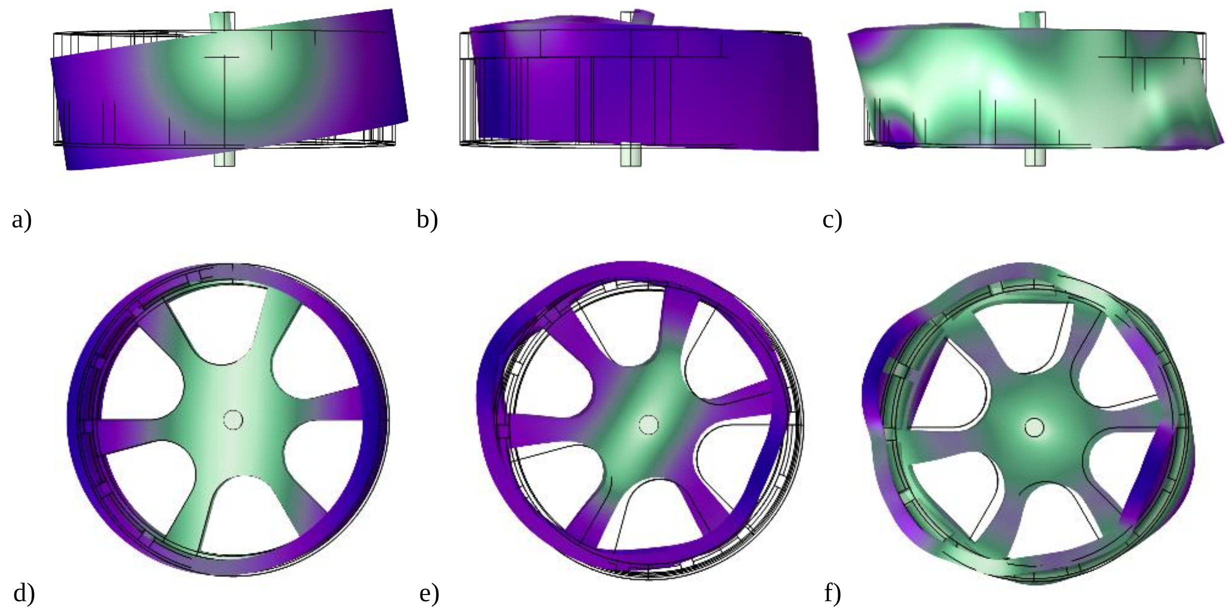

Fig. 14 Distinct mode shapes classified in the (1,1) subset (a,d) lowest frequency (b,e) middle frequency (c,f) highest frequency.

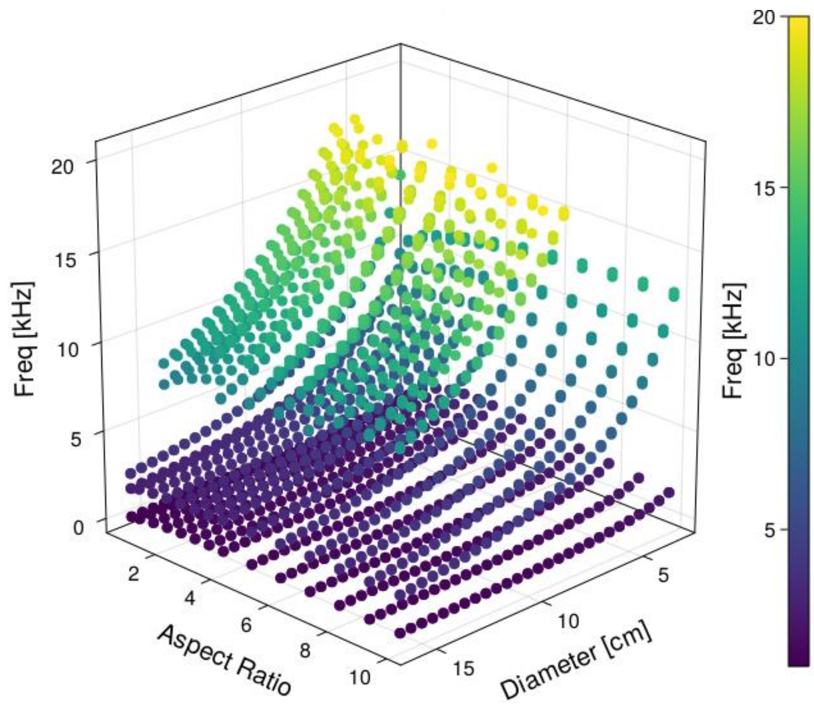

Fig. 15 Mode (1,1) parameterized sweep results for diameter, aspect ratio, and frequency dimensions.

The particular group detailed in Fig. 16 is not unique. Investigation indicates that for each of these recognizable groups, different data points within it exhibit the same particular vibration mode. Furthermore, the (1,1) mode depicted in Fig. 15 is also only one example. For most (M,N) combinations predicted by the model the member data points feature multiple distinct groups.

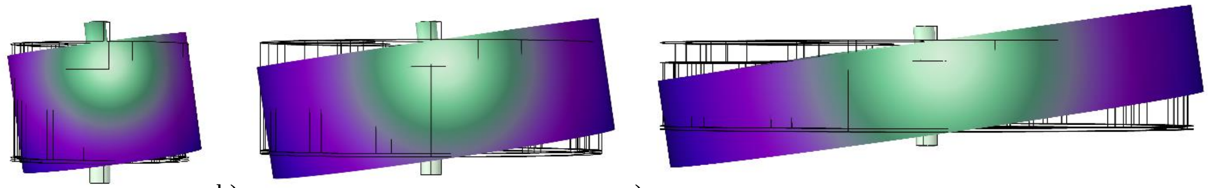
a) b) c)

Fig. 16 Rotor displacement for (a) Diameter = 5cm, Aspect Ratio = 2, (b) Diameter = 10cm, Aspect Ratio = 4, and (c) Diameter = 15cm, Aspect Ratios = 8. Approximately to scale.

D. Automatic Clustering

The structure of the points in Fig. 15 allows for the use of an automated clustering algorithm to differentiate them. While Fig. 15 shows just a 3-dimensional slice of these groups, the coherent structures extend into the entire 5-dimensional (Frequency, Diameter, Aspect Ratio, Wall Thickness Ratio, Spoke Height Ratio) data space for a given (M,N) mode with each unique resonant mode forming a coherent 5-dimensional group.

A variety of algorithms exist to automatically group points by certain spatial criteria. These algorithms use a variety of techniques to take a set of points in two or more dimensions and assign each point to a cluster based only on the spatial relationship of all the points within that space. For this analysis, the Density-Based Spatial Clustering of Applications with Noise (DBSCAN) algorithm [17] was selected. One key benefit of this algorithm is that it does not require a priori knowledge of the number of groupings. Since the number of groups varies for different (M,N) modes, the algorithm's ability to automatically determine how many groups to create reduces the manual workload.

To achieve good results using DBSCAN, normalization and scaling of the five parameters was required. This scaling was used to ensure the "radius" parameter of the DBSCAN algorithm treated distance in each dimension equally to not bias the points toward clustering more easily in any one dimension. The diameter dimension is left normalized from 0 to 1. The other three parameter values were scaled in approximate proportion to the number of samples in that dimension relative to the number of samples in the Diameter dimension. This rescaling compensates for the different spacing between sample points in different dimensions. The scaling was then tuned manually to the values shown in Table 7. to achieve good results. The scale factor on Frequency, which does not have a number of samples as it is the dependent variable, was set to three via tuning to generate satisfactory groupings.

Table 7 Scale factors applied to each dimension after normalization

Dimension	Scale Factor
Frequency	3
Diameter	1
Aspect Ratio	0.7
Wall Thickness Ratio	0.2
Spoke Height Ratio	0.2

DBSCAN has a parameter called the radius which was set to 0.125. This determines the maximum distance between points to begin linking together into a cluster. There are two other minor parameters, the minimum number of neighbors and the minimum cluster size which were set to 3 and 400 respectively. These parameters determine how interconnected several points must be to form the seed of a new cluster and the size that a new cluster must reach to be accepted. These values were tuned via trial and error.

The data from Fig. 15 is repeated in Fig. 17 but with the color of each point changed to indicate its cluster assignment. DBSCAN with tuned parameters was able to identify 3 distinct groups in the original data. DBSCAN performs well for other (M,N) modes, creating 1-4 groups as needed to separate the visibly distinct clusters.

There is one data point in Fig. 17 that is labeled "ungrouped". This is a distinct designation that is not the same as being a member of a fourth cluster. Instead, it represents a point that DBSCAN was unable to categorize into any cluster. While only one point is ungrouped in this case, some (M,N) modes have no ungrouped points while others have several dozen. In some cases, these ungrouped points have a clear qualitative connection to one of the groups, but DBSCAN does not group them because the points are too sparse. The manual parameter tuning required to achieve good results with DBSCAN is also one of its major weaknesses. Future expansions of the dataset or performing a similar analysis with motors that are different from those discussed here will require a manual retuning.

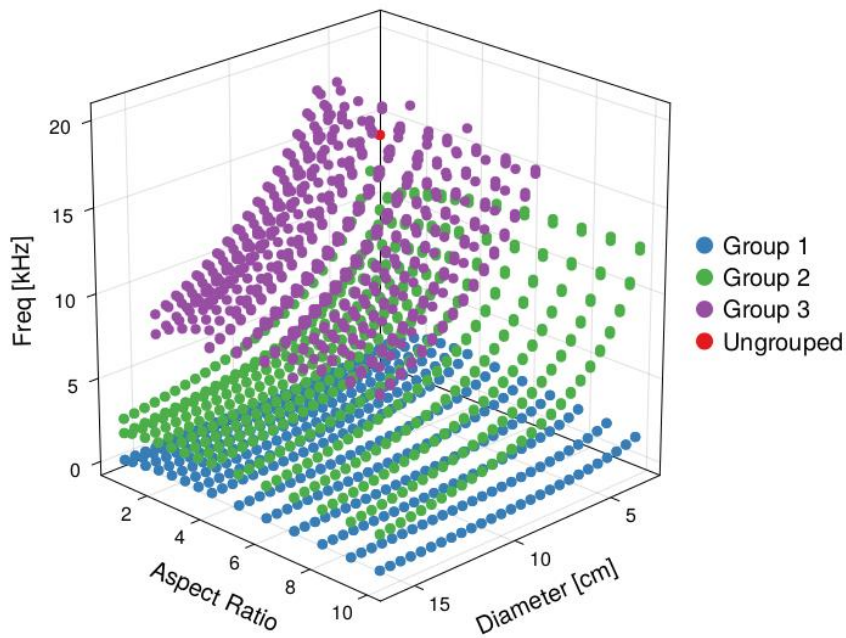

Fig. 17 Mode (1,1) parameterized sweep results for diameter, aspect ratio, and frequency dimensions. Automatically clustered into distinct groups.

E. Curve Fitting and Cluster Analysis

Fig. 18 shows each of the clusters from Fig. 17 separately. Note the different scales on the z-axes. Several observations can be made from these groups and similar groups extracted from the data for other modes. The clusters appear relatively smooth along both the Diameter and Aspect Ratio dimensions. Qualitatively, this indicates that the density of samples in the parameter space for these two dimensions is adequate to resolve their impact on mode frequencies. The minor parameters have 3 samples along each of their dimensions so there is inadequate data to assess whether they appear well resolved in the same fashion.

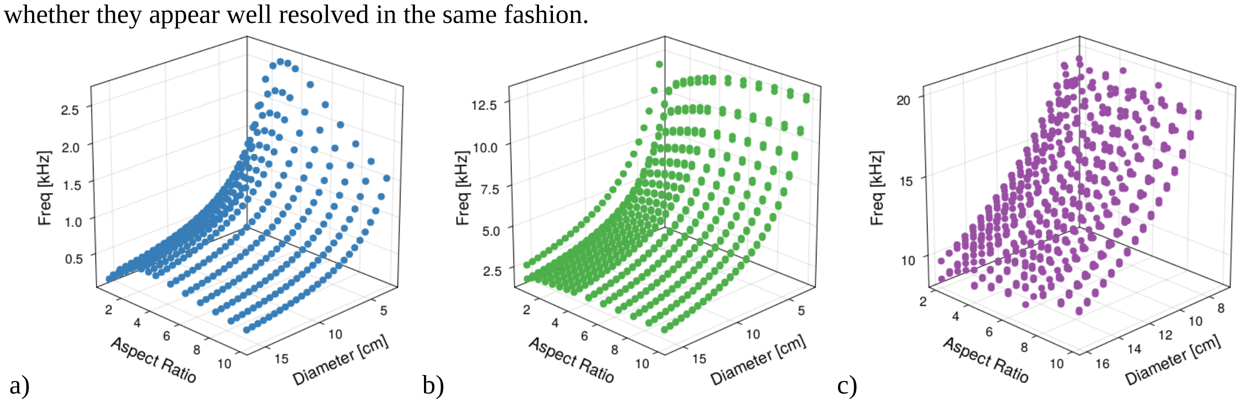

Fig. 18 Individual groups identified from the (1,1) data (a) Group 1, (b) Group 2, (c) Group 3.

The relative importance of the various parameters can also be assessed. The groups in Fig. 18 as well as the data from other modes indicate that Rotor Diameter has by far the largest impact on the mode frequency. The aspect ratio does play an important contributing factor, particularly at smaller diameters, and for groups at lower frequencies. The minor parameters have a comparatively small impact on the frequency.

A final qualitative observation is that not all groups encompass the entire parameter space. Note the smaller range of the Diameter axis for Group 3. This group is not represented at small diameters or high aspect ratios. A particular mode shape may not occur for a given combination of parameters for two different reasons, the predicted frequency may be above 20khz (the data here was filtered to only points below 20khz), or the mode may simply not be an eigenmode for a rotor with a given range of geometries. While Group 3 covers most of the parameter space, other groups for other modes are more limited. In some instances, a given group occurs at only a small fraction of the space. This will become relevant when using this data to make predictions.

The most interesting possibility with these clusters is creating a curve fit. As an initial attempt, the model described by Eq. (1) is created. The lower-case variables represent the tunable constants available to the least square fitting routine. D, AR, ST, and WT, refer to the Rotor Diameter, Aspect Ratio, Spoke Height Ratio and Wall Thickness Ratio respectively. This model was developed through trial and error. The two minor parameters are given only a linear correlation to the eigenfrequency as the three samples along each of those dimensions precludes having enough data for a more complicated relationship.

$$F = a + be^{(c*D+d)} + g(AR - h)^2 + j * AR + k * SH + l * WT \tag{1}$$

For each group, a least squares fit was performed to create a curve. This curve then predicts the frequency, for any combination of the 4 parameters, that the corresponding mode shape will have for that rotor. Repeating this process for all groups of all (M,N) subsets produces a family of curves that together can predict possible eigenmodes and eigenfrequencies for any rotor within the scope of the parameterized model. The curve fits parameters, associated eigenmodes, and other needed data are provided in Appendix I.

One important detail is the range encompassed by each group. To ensure a given curve is not used outside the region that the FEA model predicts it to occur, during the curve fit the minimum and maximum extent are recorded for each dimension. This data is stored along with the least-squares fit constants. The software implementation should ensure that a given combination of parameters lies within the region described by these limits before generating a prediction. As a result, each curve fit may predict a frequency or return nothing if that particular mode is not predicted to occur for that combination of input parameters.

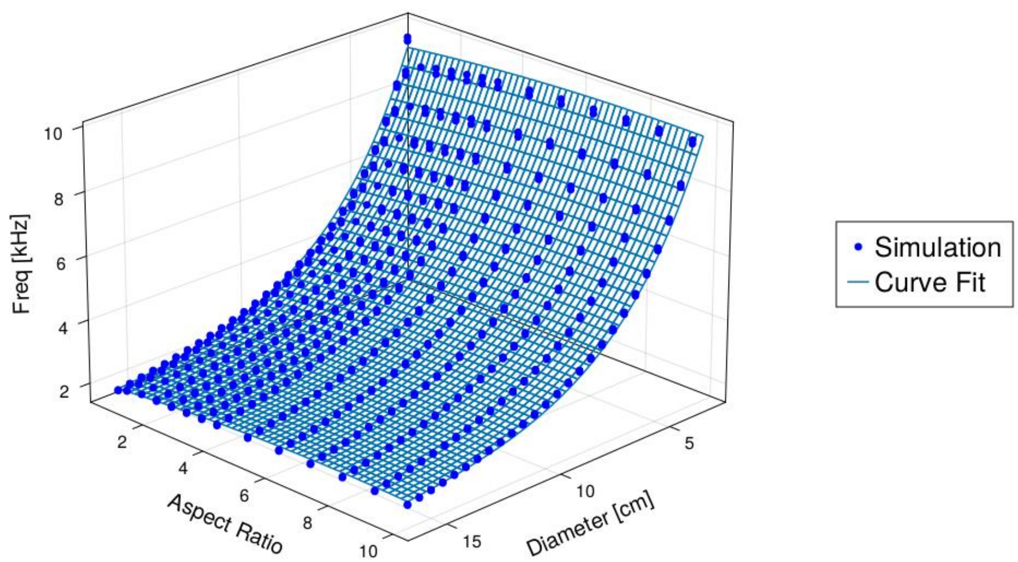

Fig. 19 Mode (1,1) Group 2 data points and least-square fitted curve.

An example of a curve fit with the corresponding data is shown in Fig. 19. This particular data is again the (1,1) Group 2 dataset also shown in Fig. 18 (b). The least squares fit model reasonably matches the source data. That said, the functional form of Equation 1 is an initial effort.

F. Experimental Modal Analysis Comparisons

Experimental modal analysis is used to identify mode shapes and corresponding frequencies of the motor rotors. By generating an animation of the motion of each accelerometer, the mode shape of each vibration can be qualitatively identified similarly to the initial FEA analysis. These displacement figures can be compared with those generated by simulation. An example of this comparison for the Scorpion rotor is shown in Fig. 20. The (3,1) mode measured experimentally corresponds to that of the simulation. The difference in rendering is due to the relatively small number of accelerometers used for the modal analysis contrasted with the high-resolution FEA analysis. Similar comparisons for other mode shapes show good qualitative agreement between experiment and simulation.

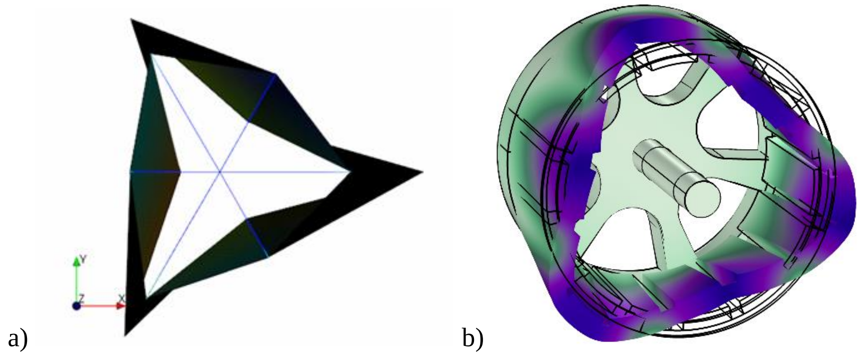

Fig. 20 Mode (3,1) rotor displacement from (a) experimental modal analysis and (b) parameterized FEA.

With the modes identified, the corresponding frequencies can be compared. Several key comparisons are shown in Table 8 for various modes occurring in the U13 rotor. The data from the modal analysis shown here is for the rotor installed onto the stator. While the simulation does not represent the stator, it is ultimately this configuration we are interested in predicting. The agreement is good for these readily identifiable mode shapes. In the case of the U13, enough accelerometers were used to distinguish even higher order modes, but these higher order modes occur at frequencies beyond the range of interest. Accurately capturing these modes is important for the modeling effort however as for other combinations of parameters these modes may enter the frequency range of interest. The (1,1) mode is not listed in Table 8. This mode is predicted by the simulation, but not detected experimentally. It is possible that this mode is suppressed by the presence of the stator.

Due to physical space constraints only six accelerometers were placed around the circumference of the Scorpion rotor and so only modes up to M=3 can be resolved as shown in

Table 9. For these modes however, agreement between simulation and experimental frequencies is reasonable if not quite as good as the U13. Again, the experimental data is of the rotor installed onto the stator. Due to the smaller size of the scorpion motor, the (0,1) mode is well beyond the frequency range of interest, but it still serves as another indication of agreement between the experiment and simulation and aids in tuning the overall model. Do note that there are a variety of modes predicted by the model and observed experimentally in the frequency range from 7kHz to 22kHz that are not listed. This is because the shape of these eigenmodes cannot be identified with the number of accelerometers used here.

Table 8 U13 Experimental mode frequencies and High-Fidelity FEA frequencies for simple modes.

Mode Shape U13	FEA frequency (Hz)	Experimental Frequency (Hz)	Percent Error
2,1	1354	1402	3.4
3,1	3273	3096	5.7
4,1	5513	5304	3.9
5,1	7434	7442	0.1
6,1	11284	10216	10.5
0,1	10702	11160	4.1

Table 9 Scorpion Experimental mode frequencies and High-Fidelity FEA frequencies for simple modes.

Mode Shape Scorpion	FEA frequency (Hz)	Experimental Frequency (Hz)	Percent Error
1,1	895	799	12.0
2,1	3120	2961	5.4
3,1	7070	6914	2.3
0,1	22460	24379	7.87

G. Acoustic Comparisons

The acoustic results for the Scorpion motor at the microphone 4 location (see Fig. 5) are shown in Fig. 21. The squares at the top of the plots show the fundamental electrical frequency and its harmonics where the fundamental electrical frequency is given by $f_1 = f_{mot}P/120$ where P is the number of poles (magnets) and f_{mot} is the motor speed in rpm. The legends indicate the motor speeds. For all speeds, the peak acoustic radiation occurs at frequencies near 3000 Hz. The peak acoustic radiation occurs at motor speeds equal to 6292 and 6441 RPM. For these motor speeds, the peak frequency occurs at the fourth electrical harmonic. The peak acoustic radiation is expected to occur at motor speeds that excite the resonance modes of the motor rotor. The peak frequencies at the 6292 and 6441 RPM are roughly 2900 Hz and 3000 Hz, respectively, and appear to align with the (2,1) mode from the FEA analysis (see

Table 9). A comparison of the acoustic radiation at microphones 7 and 4 for the Scorpion motor at 6641 RPM is shown in Fig. 22. The peak acoustic level for the 3000 Hz tone at microphone 4 is roughly 20 dB higher that that at microphone 7. The directivity for the tone is consistent with a (2,1) mode where there is little or no deflection of the motor end bell.

The acoustic radiation characteristics of the U13 motor are significantly different from those of the Scorpion motor with the U13 displaying a larger number of discrete frequencies and a very different directivity pattern than those of the Scorpion motor. The differences in the acoustic radiation are thought to be due to the significantly different aspect ratios of the two motors. As the aspect ratio increases, the end bell plays an increasingly larger role in the vibration modes and radiative surfaces. The order tracking results for the U13 motor are shown in Fig. 23. The peak acoustic radiation occurs for microphone 7 at an order close to 50. The tones radiating from the end bell of the motor are not detected in the FEA classification scheme presented here. However, many of the modes not classified had significant axial deflections of the end bell. The peak radiation for microphone 4 occurred at an order close to 170 for a motor speed near 3800 RPM which resulted in a frequency outside the range of interest for this study (over 10,000 Hz). The acoustic spectrum associated with the peaks at 3279 RPM in Fig. 23 are shown in the spectrum of Fig. 24. The tones at 1312 Hz, 2899 Hz, 5249 Hz are close to the FEA eigenfrequencies of 1354 Hz, 3273 Hz, and 5513 Hz for the (2,1), (3,1) and (4,1) modes. The tones at 3936 Hz, 6561 Hz, and in the range of 7873 – 9179 Hz are not captured in the FEA classification analysis and are expected to be associated with oscillation modes involving deflections of the motor end bell.

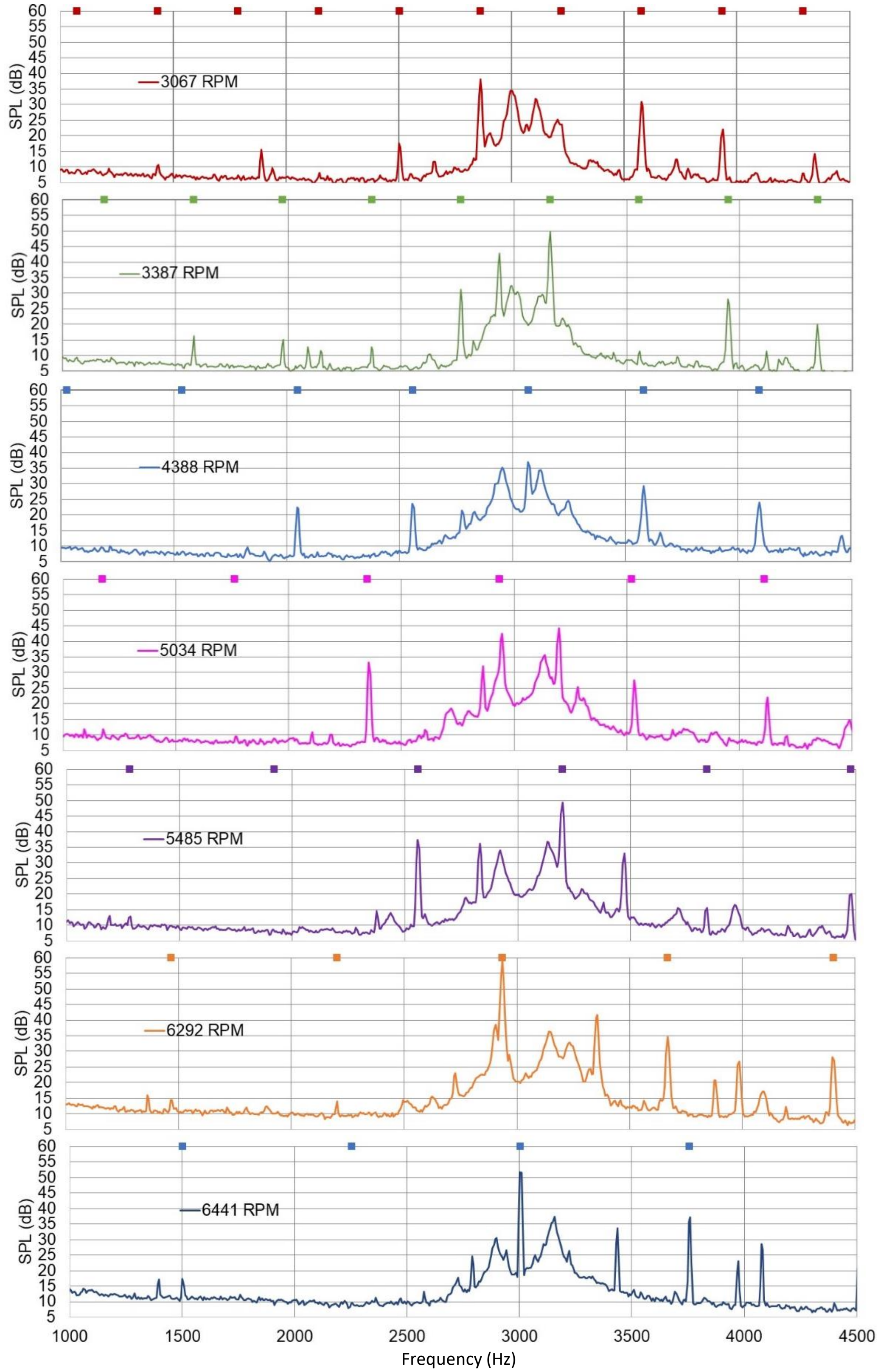

Fig. 21 Scorpion SII 4020 microphone 4 spectra at various operating speeds. Electric harmonics are indicated by squares.

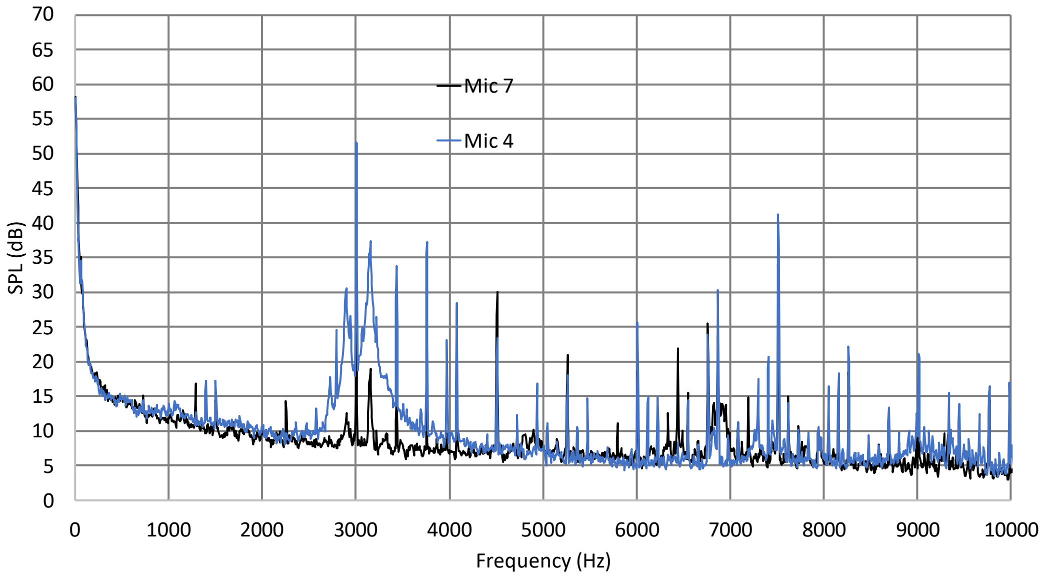

Fig. 22 Scorpion SII 4020 from motor operating at 6641 RPM directivity comparison.

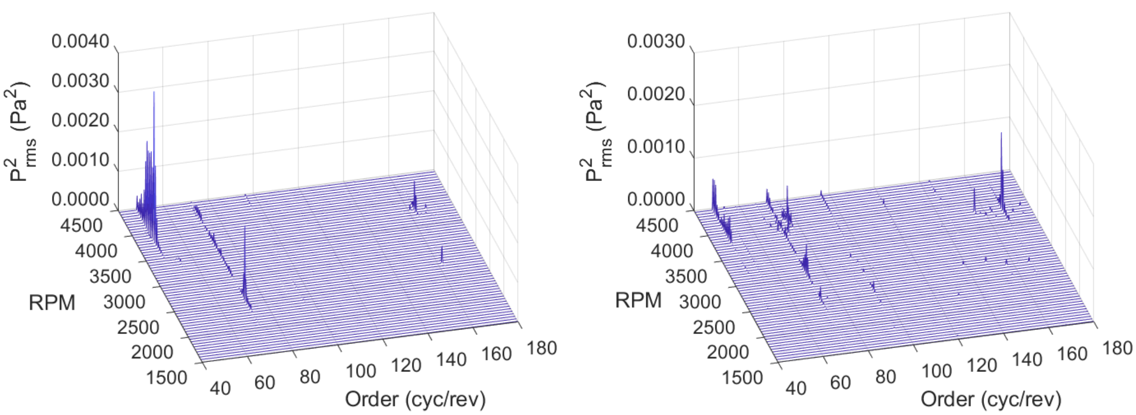

Fig. 23 U13 order tracking for microphones 7 (left) and 4 (right).

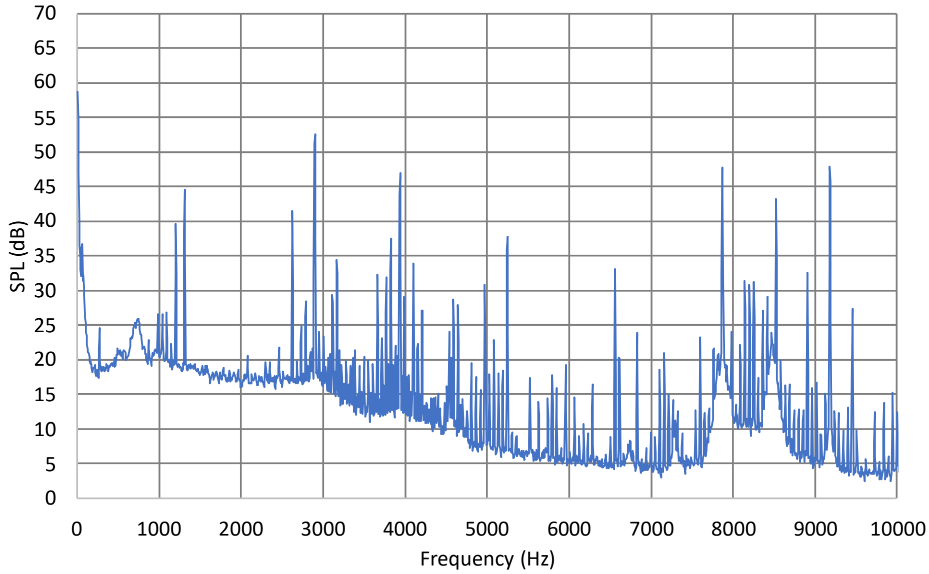

Fig. 24 U13 microphone 4 spectra from motor operating at 3279 RPM.

V. Conclusion

For brushless DC outrunner motors, there is a need to incorporate a low-fidelity electric motor model into existing noise prediction tools for future UAM vehicles. Predictions of eigenfrequencies based on analytical models of ideal cylinders do not match observed acoustic tones generated by motors used in this study. Commercially available FEA tools can predict modes and frequencies but for system-level studies, detailed motor geometries are typically unavailable. Even if a geometry were available, the computational requirements of an FEA analysis are not suitable for high-level studies where frequent design changes, rapid iteration, and exploration of a wide design space are typical.

The work reported here created an FEA informed semi-empirical model that predicts eigenmode and frequency pairs for outrunner radial flux brushless DC electric motors in the 1-5kW range. The model uses four key geometric parameters (Diameter, Aspect Ratio, Wall Thickness, and Spoke Height) of a motor's rotor to predict the eigenmodes and frequencies.

The model developed uses a series of computational analyses, each of which reduced the amount of geometric detail about the rotor and was tuned to, and validated against, experimental data. Finite element analysis was first performed on the initial high-fidelity geometric models. A simplified parameterized geometry was then created which uses only 10 geometric parameters. This model was used, via an exploration of the parameter space, to create the final semi-empirical model using the four key parameters mentioned above. In the process, an automatic clustering algorithm was used to help categorize the raw FEA data prior to the final least-squares curve fit.

The final model, when compared to experimental modal analysis, for qualitatively identical mode shapes, predicts eigenfrequencies that typically fall within the same 1/3rd octave band. This means the model is suitable for incorporation into typical high level acoustic tools such as ANOPP. Implementation of a full acoustic prediction, including an electromagnetic forcing model, acoustic propagation, and integration into ANOPP, is planned. Other avenues for future work include additional experimental validation motors, particularly for large motors to extend the applicable model range. There is also potential for investigating a larger space of parameters to optimize the selection used in the semi-empirical model. A different selection could potentially lead to increased accuracy or be needed to expand the applicable range. A comparable development technique may also be applicable to similar axial flux motors which often have very high aspect ratios.

Appendix I

a	b	c	d	g	h	j	k	l	M	N	Minimum Diameter	Maximum Diameter	Minimum Aspect Ratio	Maximum Aspect Ratio	Cluster
-0.35706	0.742387	-29.8856	1.280645	-0.01286	-0.0787	0.116555	2.568737	-1.07222	1	1	0.03	0.16	0.7	10	1
-1.09963	1.557248	-28.7851	2.036163	-0.04296	-0.1233	0.605135	2.127295	14.93248	2	1	0.03	0.16	0.7	10	2
-1.97641	1.495465	-15.4301	2.210771	-0.04445	-3.20247	1.152758	2.782811	33.22563	3	1	0.03	0.16	0.7	10	3
0.553451	1.799598	-26.2564	2.247132	-0.00749	-0.85604	0.13201	4.647509	1.162937	1	1	0.03	0.16	0.7	10	4
-2.26077	1.572869	-8.86521	2.269775	-0.04933	-6.30761	1.514688	3.29357	53.69057	4	1	0.03	0.16	0.7	10	5
2.665863	1.485503	-20.3203	2.28564	0.010095	-2.5122	-0.90075	1.357209	14.40822	0	1	0.03	0.16	0.7	3.5	6
-38.8909	3.314929	-0.82257	2.981314	-0.06057	-17.19	3.042588	3.496944	74.49383	5	1	0.045	0.16	0.7	10	7
-1.81331	1.393113	-8.5067	2.208443	1.937007	-0.95679	-5.99074	0.940119	9.959329	2	2	0.035	0.16	0.7	1.5	8
3.31393	1.549373	-18.431	2.321845	-0.00968	-10.5788	-0.35091	3.212355	13.0854	0	1	0.03	0.16	0.7	6	9
-9.68717	1.917795	-2.67663	2.455373	-0.1449	-4.88788	2.880658	2.085985	30.51465	3	2	0.04	0.16	0.7	10	10
-52.1414	1.790855	-18.5387	2.293652	0.040124	37.15896	2.319405	6.697014	5.053001	2	1	0.04	0.16	1.5	10	11
1.625185	1.399783	-10.3294	2.177604	-0.10455	-3.77121	2.114628	1.055626	55.89243	6	1	0.04	0.16	0.7	10	12
-5.6717	1.755673	-6.97046	2.331888	-0.2401	-1.25052	3.059993	1.714679	114.5761	7	1	0.07	0.16	0.7	6	13
-5.04533	2.090263	-3.32228	2.49325	-0.04264	-11.3251	1.560916	-0.42292	41.75595	0	1	0.09	0.16	1	10	14
-13.0906	2.228893	-3.22557	2.524088	-0.31543	-3.06049	4.88963	3.057416	52.40646	4	2	0.09	0.16	1.5	6	15
-111.758	5.674754	-0.29039	3.464116	-0.17898	-18.1594	8.639984	0.014178	34.69605	1	2	0.045	0.16	0.7	10	16
-27.554	1.812571	-13.4526	2.386985	-76.3404	-0.62758	229.9224	0.38414	81.56053	4	2	0.055	0.16	0.7	1	17
85.72039	1.335747	-10.3972	2.162352	-199.052	-0.22431	120.8863	1.392859	7.687621	1	2	0.065	0.16	0.7	0.7	18

Acknowledgments

This work was sponsored by the NASA Revolutionary Vertical Lift Technology (RVLT) project.

References

[1] D. L. Huff and B. S. Henderson, "Electric motor noise for small quadcopters: Part 1-Acoustic Measurements," in *2018 AIAA/CEAS Aeroacoustics Conference*, 2018.

[2] P. Vijayraghavan and R. Krishnan, "Noise in electric machines: A review," *IEEE Transactions on Industry Applications,* vol. 35, no. 5, pp. 1007-1013, 1999.

[3] Z. Q. Zhu, D. Howe, E. Bolte and B. Ackermann, "Instantaneous magnetic field distribution in brushless permanent magnet DC motors, Part I: Open-circuit field," *IEEE Transactions on Magnetics,* vol. 29, no. 1, pp. 124-135, 1993.

[4] Z. Q. Zhu and D. Howe, "Instantaneous magnetic field distribution in brushless permanent magnet DC motors, Part II: Armature-reaction field," *IEEE transactions on magnetics,* vol. 29, no. 1, pp. 136-142, 1993.

[5] Z. Q. Zhu and D. Howe, "Instantaneous magnetic field distribution in brushless permanent magnet DC motors, Part III: Effect of stator slotting," *IEEE transactions on magnetics,* vol. 29, no. 1, pp. 143-151, 1993.

[6] Z. Q. Zhu and D. Howe, "Instantaneous magnetic field distribution in permanent magnet brushless DC motors, Part IV: Magnetic field on load," *IEEE transactions on magnetics,* vol. 29, no. 1, pp. 152-158, 1993.

[7] D. Verdyck and R. J. M. Belmans, "An acoustic model for a permanent magnet machine: modal shapes and magnetic forces.," *IEEE transactions on industry applications,* vol. 30, no. 6, pp. 1625-1631, 1994.

[8] J. D. Cluts, D. L. Huff, B. S. Henderson and C. Ruggeri, "Surface Vibration Measurements and Analysis for UAM/UAS Electric Motor Noise," in *AIAA Aviation 2021 Forum*, 2021.

[9] S. Huang, M. Aydin and T. A. Lipo, "Electromagnetic vibration and noise assessment for surface mounted PM machines," in *2001 Power Engineering Society Summer Meeting*, Madison, WI, 2001.

[10] J. F. Gieras, C. Wang, J. C. Lai and N. Ertugrul, "Analytical prediction of noise of magnetic origin produced by permanent magnet brushless motors," in *IEEE International Electric Machines & Drives conference*, 2007.

[11] J. H. Leong and Z. Q. Zhu, "Acoustic noise and vibration of direct-torque-controlled permanent magnet brushless DC drive," in *6th IET International Conference on Power Electronics, Machines and Drives*, Bristol, UK, 2012.

[12] G. Dajaku and D. Gerling, "Magnetic radial force density of the PM machine with 12-teeth/10-poles winding topology," in *IEEE International Electric Machines and Drives Conference*, Maimai, FL, 2009.

[13] S. M. Castano, B. Bilgin, J. Lin and A. Emadi, "Radial forces and vibration analysis in an external-rotor switced reluctance machine.," *IET Electric Power Applications,* vol. 11, no. 2, pp. 252-259, 2017.

[14] J. F. Gieras, C. Wang and J. C. Lai, Noise of polyphase electric motors, CRC press, 2018.

[15] C. Wang and J. C. S. Lai, "Prediction of natural frequencies of finite length circular cylindrical shells," *Applied acoustics,* vol. 59, no. 4, pp. 385-400, 2000.

[16] S.-C. Huang and W. Soedel, "On the forced vibration of simply supported rotating cylindrical shells.," *The Journal of the Acoustical Society of America,* vol. 84, no. 1, pp. 275-285, 1988.

[17] M. Ester, H.-P. Kriegel, J. Sander and X. Xu, "A density-based algorithm for discovering clusters in large spatial databases with noise," in *Proceedings of the Second International Conference on Knowledge Discover and Data Mining*, Portland, Oregon, 1996.